Research article

Yida Liu[a], Jinlin Song[a], Weixian Zhao, Xuecheng Ren, Qiang Cheng, Xiaobing Luo, Nicholas Xuanlai Fang* and Run Hu*

Dynamic thermal camouflage via a liquid-crystal-based radiative metasurface

https://doi.org/10.1515/nanoph-2019-0485
Received November 28, 2019; revised February 7, 2020; accepted February 25, 2020

Abstract: Thermal camouflage, which is used to conceal objects in the infrared vision for confrontation with infrared detection in civilian or military applications, has garnered increasing attraction and interest recently. Compared with conductive thermal camouflage, that is to tune heat conduction to achieve equivalent temperature fields, radiative thermal camouflage, based on emissivity engineering, is more promising and shows much superiority in the pursuit of dynamic camouflage technology when resorting to stimuli-responsive materials. In this paper, we demonstrate the emissivity-engineered radiative metasurface to realize dynamic thermal camouflage functionality via a flying laser heat source on the metal-liquid-crystal-metal (MLCM) platform. We employ a rigorous coupled-wave algorithm to calculate the surface emissivity of Au/LC/Au microstructures, where the LC-orientation angle distribution is quantified by minimizing the emitted thermal energy standard deviation throughout the whole plate. Emissivity engineering on the MCLM platform is attributed to multiple magnetic polariton resonance, and agrees well with the equivalent electric circuit analysis. Through this electrical modulation strategy, the moving hot spot in the original temperature field is erased and a uniform temperature field is observed in the infrared camera instead, demonstrating the very good dynamic thermal camouflage functionality. The present MLCM-based radiative metasurface may open avenues for high-resolution emissivity engineering to realize novel thermal functionality and develop new applications for thermal metamaterials and meta-devices.

Keywords: thermal camouflage; mid-infrared; metasurface; liquid crystal; nanophotonics; magnetic polariton.

1 Introduction

The dynamic structural colors in the skin of chameleons and cephalopods enable them to blend into the background environment adaptively, thus they are known as the camouflage masters in the natural world [1–3]. The active color-changing feat stems from the chromatophore pigment cells and reflective cells which can operate under mechanical actuation of radial muscle and function as spectral filters to absorb and reflect visible light. The sophisticated architecture of the dynamic color-changing system has inspired the engineering of various adaptive artificial materials and devices, like optoelectronic displays, soft robots, and camouflage systems, and their working spectra have been extended beyond the visible light with many civilian and military applications [1–5]. Among them, thermal camouflage, with the aim of concealing objects from infrared (IR) imaging, has attracted increasing attention, and can be used to incapacitate IR detection [6–12]. Note that any object will radiate thermal energy whenever and wherever, thus concealing target thermal radiation for thermal camouflage is tremendously challenging.

According to the Stefan-Boltzmann law, there are two ways to tune the thermal radiation energy for thermal camouflage. One way is to change the target temperature as close as possible to approximate the background temperature when their surface emissivities are comparable, and the other way is to change the target surface emissivity to generate the same amount of emitted thermal energy as the

[a]**Yida Liu and Jinlin Song:** These authors contributed equally to this work.
***Corresponding authors: Nicholas Xuanlai Fang,** Department of Mechanical Engineering, Massachusetts Institute of Technology, Cambridge, Massachusetts 02139, USA, e-mail: nicfang@mit.edu. https://orcid.org/0000-0001-5713-629X; and **Run Hu,** State Key Laboratory of Coal Combustion, School of Energy and Power Engineering, Huazhong University of Science and Technology, Wuhan 430074, China, e-mail: hurun@hust.edu.cn. https://orcid.org/0000-0003-0274-9982
Yida Liu, Jinlin Song, Weixian Zhao, Xuecheng Ren, Qiang Cheng and Xiaobing Luo: State Key Laboratory of Coal Combustion, School of Energy and Power Engineering, Huazhong University of Science and Technology, Wuhan 430074, China. https://orcid.org/0000-0002-4370-2120 (Q. Cheng)

background. As a result, thermal camouflage can be sorted into conductive camouflage and radiative camouflage.

Conductive thermal camouflage tunes the in-plane heat conduction along a predesigned plate with anisotropic thermal conductivities for achieving an equivalent temperature profile as in a homogeneous plate outside the devices. The transformation thermotics theory and the scattering cancellation technique are frequently adopted to design such thermal metamaterials with stringent requirements of the thermal properties, like thermal conductivity and specific heat [13–24]. For the fabrication of thermal conductive metamaterials, compromise tactics are usually employed by trading off the desired performance for the fabrication feasibility, e.g. stacking the alternative-layered structures based on the effective medium approximation theory [6–8], special design of bilayer structures [9, 22, 23], or engineering phonon/defect-phonon scattering in the microscale material system by defect engineering [24], holey engineering [25], or phonon engineering [26–28]. Moreover, the in-plane heat conduction is easy to control, but sometimes hard to use in practice. For instance, though perfect thermal cloaking, camouflage, illusion functions have been achieved on plates in previous studies, we can easily observe the targets from the out-of-plane direction (z plane). Trying to fix this, a general illusion thermotics strategy has been proposed to realize conductive camouflage both in the x-y plane and the z plane, by maintaining perfect external camouflage and creating internal split illusions [6, 7]. Based on general illusion thermotics, the concept of encrypted thermal printing was proposed recently and shows the possibility to achieve a dynamic thermal illusion [8]. Conductive camouflage devices are usually excessively large to warp the target, which further limits their applications. Another key defect of most conductive camouflage is the static characteristic that once the structure and materials are designed and manufactured, the pursued thermal camouflage performances no longer function or are maintained when the target moves or the ambient environment changes.

In contrast, radiative camouflage is more promising for practical purposes since the radiative properties mainly depend on surface characteristics with broad applicability, whether the surfaces are flattened or curved, smooth or rough, rigid or flexible [29–32]. Thermal radiation can be tuned in the spectral, spatial, and polarization domains via surface emissivity engineering by nanostructures like gratings, multilayer structures, photonic crystals, metamaterials, metasurfaces, etc. [33–43]. However, most of these techniques also only suitable for static thermal camouflage. Once the structures have been laid down, it is difficult to dynamically tune the thermal emission from the nanostructured surfaces. To date, only a very limited number of studies report dynamic thermal camouflage due to the stringent requirement and challenging implementation [1]. Fortunately, dynamic control of thermal radiation can be achieved by introducing responsive materials that can change their thermal radiation under external stimuli like electrics, magnetics, heat, mechanics, etc. [30–37]. These stimuli-responsive materials enable us to achieve dynamic thermal camouflage to pursue the final goal like camouflage masters in nature. Compared to other external stimuli, electrical modulation is more flexible, fast, and reliable, thus attracting more attention recently, and has been successively applied onto quantum wells, graphene, biomimetic materials for thermal camouflage applications. Among these possibilities, nematic liquid crystals (LCs), as a family of stimuli-responsive materials, also show great potential for electrically controlling thermal radiation due to their inherently high optical anisotropy, low power consumption, easy controllability of LC particle orientation, sub-millisecond response time, and high compatibility with almost all optoelectronic materials [44–48]. LCs can also be integrated into metal-insulator-metal gratings, in which the insulator layer is composed of LCs, to construct a dynamic platform that powerfully combines the physics flexibility of a metal-insulator-metal framework and precise tunability of LCs, with applications like waveguides, filters, and resonators [49, 50]. Nevertheless, such a dynamic platform has never been explored for thermal camouflage feasibility.

In this paper, we propose a general strategy to dynamically tune the thermal emission from a metal-liquid-crystal-metal (MLCM) radiative metasurface for dynamic thermal camouflage. The rigorous coupled-wave algorithm (RCWA) method is employed to calculate the surface emissivity with varying the director-axis orientation angle of LCs. The MLCM unit cells can be controlled independently to achieve different amounts of thermal radiation energy, and the orientation angles and emissivities of the whole metasurface are screened by achieving the same amount of thermal radiation energy for the same detected temperature, though at different real temperatures. A more vivid demonstration is presented on the MLCM metasurface when a flying laser heat source is moving on the bottom of the MLCM platform; a uniform detected temperature field is maintained by the proposed strategy, verifying the dynamic thermal camouflage performance.

2 Results and discussion

The schematic of the proposed MLCM microstructure is shown in Figure 1. The grating ridge is made of gold

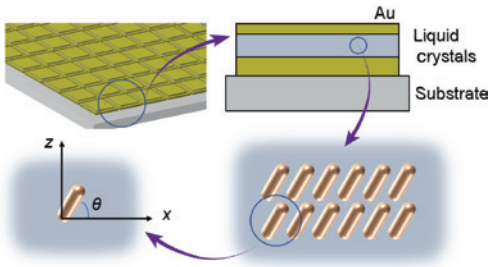

Figure 1: Schematic of the metal-liquid-crystal-metal (MLCM)-based metasurface architecture, in which the liquid crystal (LC) layer with a thickness of 0.2 μm is underneath the gold thin layer with thickness of 0.01 μm, respectively.
The orientation angle θ_{LC} of the crystals in liquids can be adjusted by the input voltage dynamically.

(Au) and LC patches with thicknesses of $d_1 = 0.01$ μm and $d_2 = 0.2$ μm. The periodic arrays of patches are deposited on an opaque Au substrate with a thickness of $d_3 = 0.5$ μm, so that the transmittance can be neglected. The period Λ is fixed as 3 μm, and the grating width w is set as 2.4 μm.

The dielectric function of gold is modeled by the Drude model $\varepsilon_{Au} = 1 - \frac{\omega_p^2}{\omega(\omega + i\gamma)}$, where $\omega_p = 1.37 \times 10^{16}$ rad/s and $\gamma = 3.66 \times 10^{13}$ rad/s are the plasmon frequency and damping parameter, respectively. The permittivity of the LC layer is given by $\varepsilon_{LC} = \frac{\varepsilon_{\parallel}\varepsilon_{\perp}}{\varepsilon_{\parallel}\cos^2\theta + \varepsilon_{\perp}\sin^2\theta}$, in which $\varepsilon_{\parallel} = 4$ and $\varepsilon_{\perp} = 2$ refer to the permittivities for light polarized parallel and perpendicular, respectively [49, 50]. The ε_{LC} exhibits independence of frequency and only relies on the director axis orientation angle θ_{LC} with respect to the wavevector [51]. The RCWA method, developed to numerically solve the Maxwell equations for determining the radiative properties of periodic structures, is used to calculate the wavelength-dependent reflectance R_λ and transmittance T_λ with considering a total of 101 diffraction orders [52]. According to Kirchhoff's law with an opaque substrate, the wavelength-dependent surface emissivity is obtained as $\varepsilon_\lambda = 1 - R_\lambda$.

The emissivity spectra with varied orientation angles from 0° to 90° in the wavelength range from 6 μm to 20 μm are shown in Figure 2A. It can be seen that with the linear increase of orientation angle from 0° to 90°, the peak of the emissivity spectrum is red-shifted from ~8.7 μm to ~11.8 μm, and the emissivity intensity also increases from 0.81 to 0.98. These peaks originate from magnetic polaritons (MPs) supported by the MLCM structure, demonstrated by the magnetic field distribution at the MP resonance wavelength. Note that MPs cannot be excited for transverse electric waves for one-dimensional microstructures [53, 54], the electric fields of which are parallel to the groove direction. Therefore, only transverse magnetic waves are considered here. Here, MPs refer to the strong coupling of the magnetic resonance in MLCM structures with external electromagnetic fields, corresponding to high surface emissivity. It is noteworthy that the emissivity range can be further expanded for better performance via optimization in terms of structure and material, for example, choosing LC E7 with a broader tunable permittivity range ($\varepsilon_{\parallel} = 19$ and $\varepsilon_{\perp} = 5$) in different directions [55, 56]. Figure 2B presents the magnetic field distribution at 8.7 μm with $\theta_{LC} = 0°$. The white lines denote the profile of the MLCM structure. The contour shows the magnetic field intensity in the y direction, i.e. $|Hy|^2$. It can be observed that the strong magnetic field is confined in the LC layer, which demonstrates the excitation of MPs and corresponds to the high emissivity peak in Figure 2A. As we know, MPs resonance wavelengths can also be predicted by an inductor-capacitor circuit theory [57–59]. According to Lenz's law, due to the time-varying magnetic field in the y direction, an oscillating current can form a loop which endows the MLM structure with diamagnetism, via generating a reversed magnetic field. In order to further demonstrate the excitation of MPs, Figure 2C gives the equivalent circuit for the MLCM structure, in which the arrows point out the direction of electric currents. In the equivalent circuit model, L_m, expressed as $L_m = 0.5\,\mu_0 w d_2/l$ where μ_0 is the permeability of vacuum and l is the patch length in the y direction, denotes the parallel-plate inductance separated by the intermediate LC layer. $C_g = \varepsilon_0 d_1 l/(\Lambda - w)$ refers to the capacitance accounting for the gap between the neighboring Au ridges, where ε_0 is the permittivity of vacuum. $C_m = c_1 \varepsilon_{LC} \varepsilon_0 w l/d_2$ is the parallel-plate capacitance between two layers because of the existence of the LC layer, where $c_1 = 0.2$ is a numerical factor that considers non-uniform charge distribution. Drifting electrons also contribute much to the total inductance in this MLCM structure, and the kinetic inductance is calculated from $L_e = -w/(\omega^2 d_{eff} l \varepsilon_0 \varepsilon'_{Au})$, where ω is the angular frequency, ε'_{Au} is the real part of the dielectric function of Au which can be obtained from the Drude model, and d_{eff} is the effective thickness for electric currents in the Au layer as $d_{eff} = \begin{cases} \delta, & \delta < d_2 \\ d_2 \end{cases}$, where the power penetration depth $\delta = \lambda/4\pi\kappa$, with λ the incident wavelength and κ the extinction coefficient of Au. So the total impedance of this inductor-capacitance circuit can be expressed as [57–59]:

$$Z_{tot} = \frac{i\omega(L_m + L_e)}{1 - \omega^2(L_m + L_e)C_g} + i\omega(L_m + L_e) - \frac{2i}{\omega C_m} \quad (1)$$

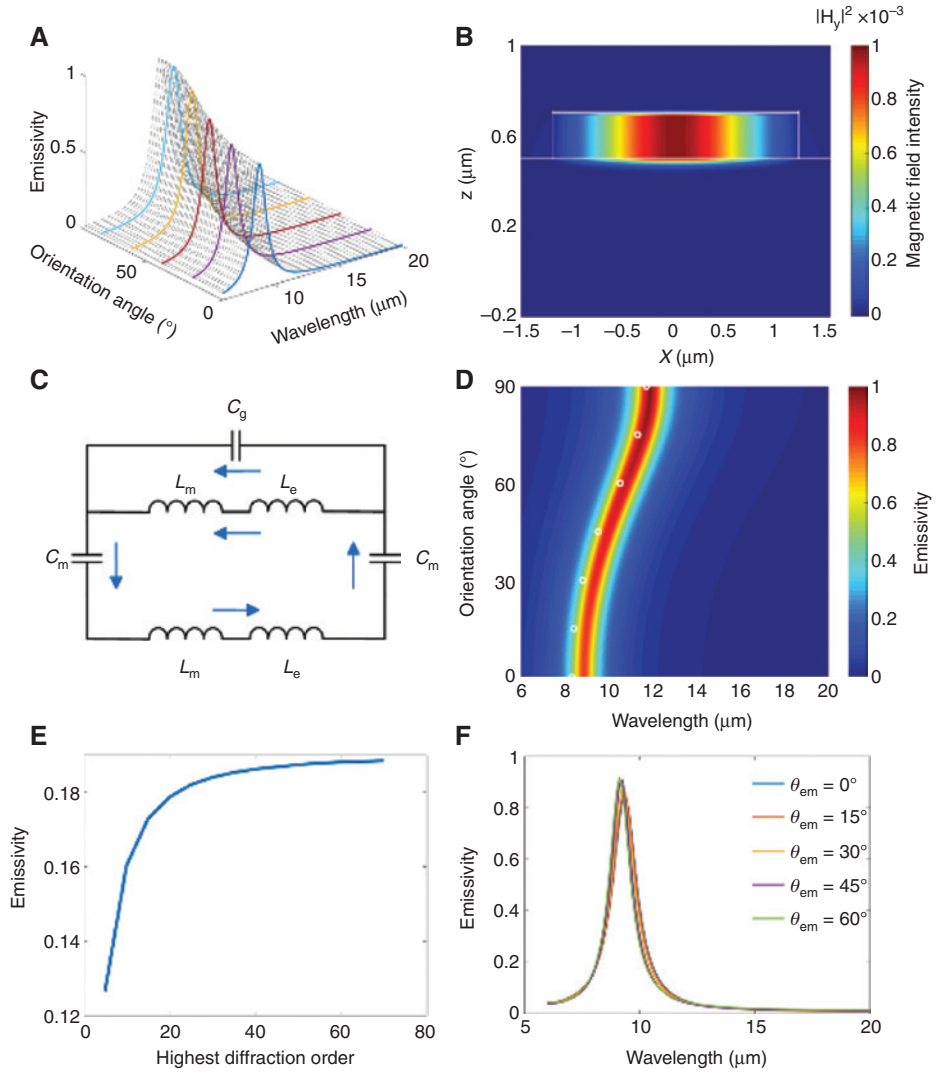

Figure 2: Emissivity spectra, physical explanations, and directional dependence of the MLCM metasurface.
(A) Rigorous coupled-wave algorithm (RCWA)-predicted emissivity spectra in terms of wavelength and orientation angle. (B) Magnetic field distribution at 8.7 μm when $\theta_{LC} = 0°$. (C) Equivalent inductor-capacitor circuit model for the metal-liquid-crystal-metal (MLCM) structure with the arrows denoting the direction of electric currents. (D) Emissivity spectra with varied orientation angles from 0° to 90°. The circles show the predicted values of resonance wavelengths by the equivalent circuit model. (E) Convergence of emissivity as a function of highest diffraction order at wavelength of 10 μm. (F) Dependence of emissivity spectra on the detecting angle θ_{det} when $\theta_{LC} = 30°$.

Then, the MP resonance condition can be solved by setting $Z_{tot} = 0$. Using the equivalent circuit theory, for example, resonance wavelengths at $\theta_{LC} = 0°$, 45° and 90° can be obtained as $\lambda_R = 8.3$ μm, 9.5 μm and 11.7 μm, which match well with the RCWA results of 8.7 μm, 9.8 μm and 11.8 μm, as shown in Figure 2D, strongly demonstrating the excitation of MPs. The accuracy of the RCWA method depends solely on the number of terms in the field space-harmonic Fourier expansion, which can be directly obtained by the highest diffraction order [60]. Therefore, one can validate the results by simply investigating the effects of the highest diffraction order [61–64]. As shown in Figure 2E, the emissivity changes within 0.6% when the highest diffraction order increases from 50 to 70, demonstrating that the highest diffraction order of 50 (corresponding to a total of 101 diffraction orders) is enough for accurate calculation. The emissivity spectra in Figure 2F are maintained even when the detected plane is rotated by $\theta_{det} = 60°$, which verifies good angle independence.

The integrated radiation power in the working wavelength range 8 ~ 13 μm differs greatly due to the wavelength-shift of the emission peak. Such series of different emissivity spectra and their corresponding orientation angles of LCs, acting as the basic database, allow us to flexibly tune the surface with a certain temperature

distribution to achieve the desired pseudo temperature for dynamic thermal camouflage. A flying laser is pumped onto the bottom of a 100 mm×100 mm×5 mm silicon plate to generate dynamic temperature distributions, as shown in Figure 3A. All the surfaces are naturally cooled with a constant convective heat transfer coefficient of 2 W/(m^{2}K) at a room temperature of 293 K. The laser point is moving with a total input power P_{total} of 10 watt and a radius R of 5 mm at a velocity v of 1 mm/s. The peak heat flux intensity $q_0 = 2P_{total}/(\pi R^2)$. The mathematical description of the non-uniform circular heat source is $q(x, y, t) = q_0\left(1 - \frac{(x - vt - x_0)^2 + (y - y_0)^2}{R^2}\right)$ within the circular region with radius R. Here, x and y denote the x-coordinate and y-coordinate, respectively, within the plate domain, t is the time, and (x_0, y_0) is the coordinate of the start point. With movement of the laser heat source, the temperature profile on the top surface of the silicon plate will change dynamically, and now we aim to thermally camouflage the moving heat source from the above

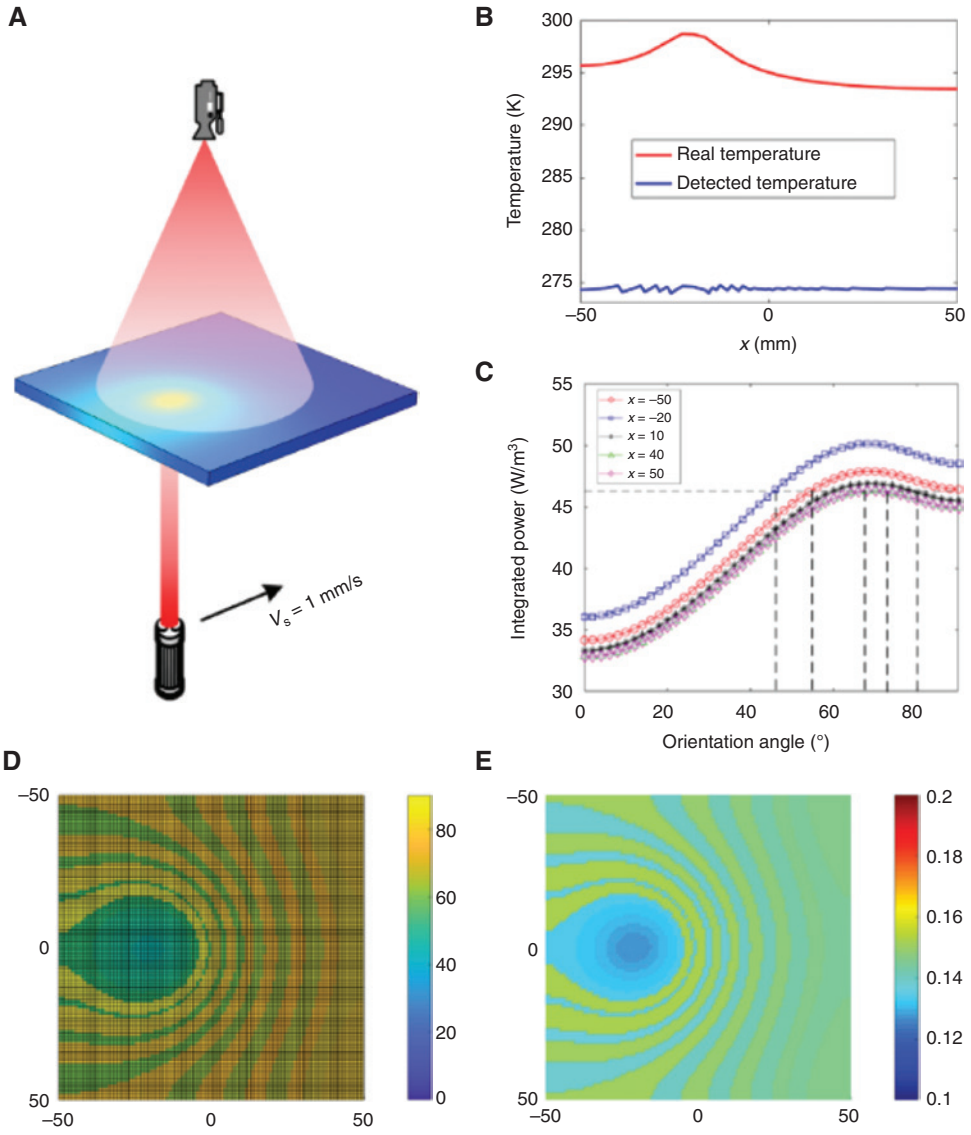

Figure 3: Radiative liquid crystal (LC)-based metasurface design process for thermal camouflage.
(A) Schematic of the demonstration setup, in which a moving heat source is achieved by a flying laser point, and an IR camera is used to detect the top surface temperature of a silicon plate. (B) Real and detected temperature curve along the x-axis of the simulated plate with the moving heat source at 10 s. (C) Integrated radiation power with varied orientation angle of five typical unit cells along the x-axis at this moment. A proper radiation power is selected by minimizing the standard deviation (STD) of the integrated radiation power of all unit cells on the simulated plate. The corresponding orientation angles of the typical five unit cells can be quantified as the vertical dash lines denote. (D) Optimized orientation angle distribution and (E) corresponding emissivity distribution throughout the simulated plate at this moment.

IR camera dynamically. The real temperature is obtained by finite-element method (FEM) simulations. For simplification, the laser heat source only moves along the *x*-axis and thus the y-coordinate is zero. The start point can be adjusted at will, and here the coordinate of the start point is (–30, 0) mm. In the FEM simulations, all the surfaces are immersed in air with a natural air convective coefficient of 2 W/(m^2 · K) at a room temperature of 293 K.

At $t = 10$ s, the laser heat source moves to (–20, 0) mm; the temperature profile along the *x*-axis is shown in Figure 3B and the 3D temperature field is shown in Figure 4A. The real temperature curve in Figure 3B is obtained by transient FEM simulations. It is seen that the location with projected by the laser heat source has the maximum temperature, and due to the asymmetry, the temperature profile is not symmetric in terms of the *y*-axis. The maximum temperature along the centre line is 298.71 K and the boundary is at 295.66 K. To thermally camouflage the heat source with emissivity engineering, we divide the top surface into $M \times N$ unit cells, and on each unit cell, we deposit different MLCM structures with different LC orientation angles. According to Planck's law, the integrated radiation power is calculated as:

$$P = \int_8^{13} \varepsilon_\lambda E_{b\lambda} d\lambda = \int_8^{13} \varepsilon_\lambda \frac{C_1 \lambda^{-5}}{e^{C_2/(\lambda T_o)} - 1} d\lambda \quad (2)$$

where $C_1 = 3.743 \times 10^{-16}$ W · m^3 and $C_2 = 1.4387 \times 10^{-2}$ m · K are the two Planck constants. Figure 3C shows the integrated radiation power variation of five typical unit cells along the *x*-axis of the plate with different orientation angles. It is seen that the integrated radiation power shares similar dependence on the orientation angles and higher temperature (blue square) corresponds to higher radiation power in general. The detected temperature is obtained by interpreting the equivalent integrated power in Figure 3C over the area-averaged emissivity according to Planck's law. Though the local temperature of each unit cell is different, we tune the emissivity one by one to make the integrated radiation power of all the unit cells at the desired same/approximate level of P_d, as denoted by the dash line in Figure 3C, which can be detected at the same pseudo temperature in the IR camera, and thermal camouflage is achieved. We screen the orientation angle in each unit cell to maintain the standard deviation (STD) σ of all the integrated radiation power as minimum as possible by $\sigma = \sqrt{\sum_{k=1}^{k=M\times N} (P_k - P_d) / (M \times N)}$. To quantify P_d, we decrease the P_d gradually and calculate the corresponding STD until the STD is the minimum globally. By such a method, the P_d is quantified as $P_d = 46.267$ W/m^3, and the orientation angles of all the unit cells are selected one by one, denoted by the vertical dash lines in Figure 3C. The

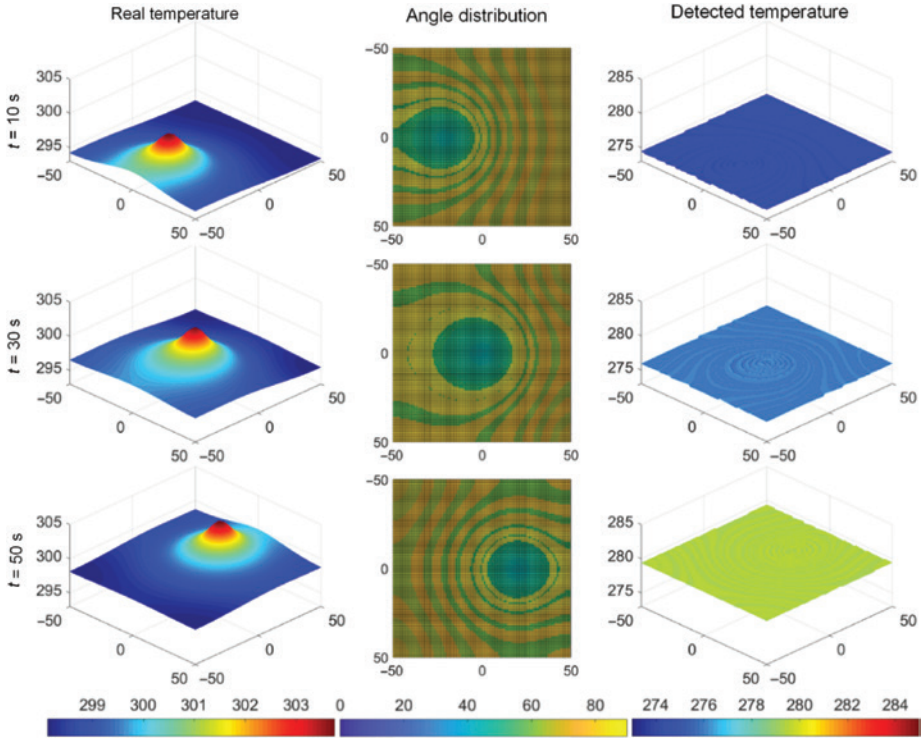

Figure 4: Demonstration of dynamic thermal camouflage via the radiative liquid crystal (LC)-based metasurfaces, including the real temperature, angle distribution, and the detected temperature at 10 s, 30 s, and 50 s.

specific orientation angles throughout the plate at this moment are shown in Figure 3D, and the corresponding emissivity distribution is shown in Figure 3E. It is seen that the distributions of the orientation angles and the corresponding emissivity fluctuate from the heat source region to the boundary. In particular, the orientation angles of the heat source region are relatively small, with relatively low emissivity, otherwise the integrated radiation energy may be hard to be consistent with that at the boundary region. By pre-setting a constant surface emissivity in the IR camera as the average emissivity value of the all the unit cells, the detected temperature field can be obtained according to the Stefan-Boltzmann law and the temperature curve along the *x*-axis is shown in Figure 3B. Compared with the real temperature curve, the observed one is much more uniform and the temperature deviation is within ±0.4 K, demonstrating the successful erasing of the heat source from the IR image.

To demonstrate the dynamic thermal camouflage, we move the laser heat source from the start point (–30, 0) mm with a constant velocity at 1 mm/s along the *x*-axis. The temporal temperature fields at 10 s, 30 s, and 50 s are shown in Figure 4. It is seen that the hot spot is moving along with the laser heat source naturally, and although the laser heat source is circular, the local temperature field is not symmetric in terms of the circular centre. This is because of the residual effect of heat conduction by the moving heat source. Following the above explained algorithm, the temporal orientation angle distributions at the corresponding time steps are also shown in Figure 4. The relatively low orientation angles in the heat source region are clearly illustrated, from which we also can identify the moving of the heat source. Due to the same reason for the asymmetric temperature field, the angle distribution is also asymmetric in terms of the circular centre. The highlight is seeing the detected temperature field at different time steps. It is seen that although the real temperature fields are not uniform from which we can identify the laser heat source easily, what we can see from the IR camera is only a uniform temperature and we cannot identify the heat source any more, demonstrating dynamic thermal camouflage.

The primary idea in this paper is to engineer the surface emissivity distribution to realize dynamic thermal camouflage functionality. The performance of the present functionalities can be further improved, such like the uniformity of the detected temperature, if we can construct a larger database of the optional surface emissivity with varied orientation angles, or resort to a broader tunable permittivity range. The present method is also effective for larger plates, a higher input power, more complicated moving paths, etc. We can also extend to MLCM structures of other materials, e.g. refractory materials like tungsten, for very high temperature applications.

3 Conclusion

In summary, we demonstrate the feasibility of a radiative MLCM metasurface consisting of Au/LC/Au gratings to realize thermal camouflage by structuring the surface emissivity. Owing to the excitation of MPs supported by the grating, its emission spectrum exhibits a high peak with high tunability through tuning the orientation angle of LCs. The emission spectra of the Au/LC/Au gratings are calculated by the RCWA algorithm with varied LC orientation angles, which generate the MLCM database for surface microstructure optimization. The proper orientation angle distribution is quantified by minimizing the temperature standard deviation on the whole plate. Through this strategy, the hot spot in the original temperature field is erased and the observed temperature field is much more uniform with a temperature difference deviation as low as ±0.4 K. A uniform temperature rather than the non-uniform real temperature is detected, which can be used to mislead the IR camera for thermal camouflage functionality. The present radiative LC-based metasurface may open avenues for emissivity engineering to realize more novel thermal functionalities and develop new applications for thermal metamaterials and meta-devices.

Acknowledgements: The authors would like to acknowledge the financial support from the National Natural Science Foundation of China (Grant numbers 51606074, 51625601, 51806070), the Ministry of Science and Technology of China (Project number 2017YFE0100600), and the China Postdoctoral Science Foundation (2018M632849).

Conflicts of interest: There are no conflicts of interest to declare.

References

[1] Xu C, Stiubianu GT, Gorodetsky AA. Adaptive infrared-reflecting systems inspired by cephalopods. Science 2018;359:1495–500.
[2] Morin SA, Shepherd RF, Kwok SW, et al. Camouflage and display for soft machines. Science 2012;337:828–32.
[3] Yu C, Li Y, Zhang X, et al. Adaptive optoelectronic camouflage systems with designs inspired by cephalopod skins. Proc Natl Acad Soc 2014;111:12998–3003.

[4] Wang GP, Chen X, Liu S, et al. Mechanical chameleon through dynamic real-time plasmonic tuning. ACS Nano 2016;10:1788–94.
[5] Chen Y, Duan X, Matuschek M, et al. Dynamic color displays using stepwise cavity resonators. Nano Lett 2017;17:5555–60.
[6] Hu R, Zhou S, Li Y, et al. Illusion thermotics. Adv Mater 2018;30:1707237.
[7] Zhou SL, Hu R, Luo XB. Thermal illusion with twinborn-like heat signatures. Int J Heat Mass Transfer 2018;127:607–13.
[8] Hu R, Huang S, Wang M, et al. Encrypted thermal printing with regionalization transformation. Adv Mater 2019;31:1807849.
[9] Han TC, Bai X, Thong JTL, et al. Full control and manipulation of heat signatures: cloaking, camouflage and thermal metamaterial. Adv Mater 2014;26:1731–4.
[10] Hou QW, Zhao XP, Meng T, et al. Illusion thermal device based on material with constant anisotropic thermal conductivity for location camouflage. Appl Phys Lett 2016;109:103506.
[11] Li Y, Bai X, Yang T, et al. Structured thermal surface for radiative camouflage. Nat Commun 2018;9:273.
[12] Peng X, Hu R. Three-dimensional illusion thermotics with separated thermal illusions. ES Energy Environ 2019;6:39–44.
[13] Fan CZ, Gao Y, Huang JP. Shaped graded materials with an apparent negative thermal conductivity. Appl Phys Lett 2008;92:251907.
[14] Guenneau S, Amra C, Veynante D. Transformation thermodynamics: cloaking and concentrating heat flux. Opt Express 2012;20:8207–18.
[15] Narayana S, Sato Y. Heat flux manipulation with engineered thermal materials. Phys Rev Lett 2012;108:214303.
[16] Hu R, Huang S, Wang M, et al. Binary thermal encoding by energy shielding and harvesting units. Phys Rev Appl 2018;10:054032.
[17] Schittny R, Kadic M, Guenneau S, et al. Experiments on transformation thermodynamics: Molding the flow of heat. Phys Rev Lett 2013;110:195901.
[18] Hu R, Xie B, Hu JY, et al. Carpet thermal cloak realization based on the refraction law of heat flCa. EPL 2015;111:54003.
[19] Hu R, Wei XL, Hu JY, et al. Local heating realization by reverse thermal cloak. Sci Rep 2014;4:3600.
[20] Choe HS, Prabhakar R, Wehmeyer G, et al. Ion write micro-thermotics: programing thermal metamaterials at the microscale. Nano Lett 2019;19:3830–7.
[21] Hu R, Luo XB. Two-dimensional phonon engineering triggers microscale thermal functionalities. Nat Sci Rev 2019;6:1071–3.
[22] Han TC, Bai X, Gao DL, et al. Experimental demonstration of a bilayer thermal cloak. Phys Rev Lett 2014;112:054302.
[23] Xu H, Shi X, Gao F, et al. Ultrathin three-dimensional thermal cloak. Phys Rev Lett 2014;112:05430.
[24] Huang S, Zhang J, Wang M, Hu R, Luo X. Macroscale thermal diode-like black box with high transient rectification ratio. ES Energy Environ 2019;6:51–6.
[25] Zhao YS, Liu D, Chen J, et al. Engineering the thermal conductivity along an individual silicon nanowire by selective helium ion irradiation. Nat Commun 2017;8:15919.
[26] Lee J, Lee W, Wehmeyer G, et al. Investigation of phonon coherence and backscattering using silicon nanomeshes. Nat Commun 2017;8:14054.
[27] Ye ZQ, Cao BY. Nanoscale thermal cloaking in graphene via chemical functionalization. Phys Chem Chem Phys 2016;18:32952.
[28] Liu YD, Cheng YH, Hu R, et al. Nanoscale thermal cloaking by in-situ annealing silicon membrane. Phys Lett A 2019;383:2296–301.
[29] Song J, Huang S, Ma Y, et al. Radiative metasurface for thermal camouflage, illusion and messaging. Opt Express 2020;28:875–85.
[30] Xiao L, Ma H, Liu J, et al. Fast adaptive thermal camouflage based on flexible VO2/Graphene/CNTN thin films. Nano Lett 2015;15:8365–70.
[31] Salihoglu O, Uzlu HB, Yakar O, et al. Graphene based adaptive thermal camouflage. Nano Lett 2018;18:4541–8.
[32] Moghimi MJ, Lin G, Jiang HR. Broadband and ultrathin infrared stealth sheets. Adv Eng Mater 2018;20:1800038.
[33] Baranov EG, Xiao Y, Nechepurenko IA, et al. Nanophotonic engineering of far-field thermal emitters. Nat Mater 2019;18:920–30.
[34] Qu Y, Li Q, Cai L, et al. Thermal camouflage based on the phase-changing material GST. Light: Sci Appl 2018;7:26.
[35] Dyakov SA, Semenenko VA, Gippius NA, et al. Magnetic field free circularly polarized thermal emission from a chiral metasurface. Phys Rev B 2018;98:235416.
[36] Marquier F, Arnold C, Laroche M, et al. Degree of polarization of thermal light emitted by gratings supporting surface waves. Opt Express 2008;16:5305–13.
[37] Lee N, Kim T, Lim JS, et al. Metamaterial selective emitter for maximizing infrared camouflage performance with energy dissipation. ACS Appl Mater Interfaces 2019;11:21250–57.
[38] Greffet JJ, Carminati R, Joulain K, et al. Coherent emission of light by thermal sources. Nature 2002;416:61–4.
[39] Liu XL, Tyler T, Starr T, et al. Taming the blackbody with infrared metamaterials as selective thermal emitters. Phys Rev Lett 2011;107:045901.
[40] Liu X, Padilla WJ. Reconfigurable room temperature metamaterial infrared emitter. Optica 2017;4:430–3.
[41] Coppens ZJ, Valentine JG. Spatial and temporal modulation of thermal emission. Adv Mater 2017;29:1701275.
[42] Xie X, Li X, Pu M, et al. Plasmatic metasurfaces for simultaneous thermal infrared invisibility and holographic illusion. Adv Funct Mater 2018;28:1706673.
[43] Cui YX, Fung KH, Xu J, et al. Ultrabroadband light absorption by a sawtooth anisotropic metamaterial slab. Nano Lett 2012;12:1443–7.
[44] Shen ZX, Zhou SH, Ge SJ, et al. Liquid crystal enabled dynamic cloaking of terahertz Fano resonators. Appl Phys Lett 2019;114:041106.
[45] Shen Z, Zhou S, Ge S, et al. Liquid-crystal-integrated metadevices: towards active multifunctional terahertz wave manipulations. Opt Lett 2018;43:4695–8.
[46] Chen P, Ma LL, Hu W, et al. Chirality invertible superstructure mediated active planar optics. Nat Commun 2019;10:2518.
[47] Khoo IC. Nonlinear optics of liquid crystalline materials. Phys Rep 2009;471:221–67.
[48] Borshch V, Shiyanovskii SV, Lavrentovich OD. Nanosecond electro-optic switching of a liquid crystal. Phys Rev Lett 2013;111:107802.
[49] Werner DH, Kwon DH, Khoo IC. Liquid crystal clad near-infrared metamaterials with tunable negative-zero-positive refractive indices. Opt Express 2007;15:3342–7.
[50] Zografopoulos DC, Beccherelli R. Liquid-crystal-tunable metainsulator-metal plasmonic waveguides and Bragg resonators. J Opt 2013;1:055009.

[51] Khoo C, Werner DH, Liang X, et al. Nanosphere dispersed liquid crystals for tunable negative-zero-positive index of refraction in the optical and terahertz regimes. Opt Lett 2006;31:2592–4.
[52] Li LF. Formulation and comparison of two recursive matrix algorithms for modeling layered diffraction gratings. J Opt Soc Am A 1996;13:1024–35.
[53] Wang LP, Zhang ZM. Resonance transmission or absorption in deep grating explained by magnetic polaritons. Appl Phys Lett 2009;95:111904.
[54] Wang LP, Zhang ZM. Wavelength-selective and diffuse emitter enhanced by magnetic polaritons for thermophotovoltaics. Appl Phys Lett 2012;100:063902.
[55] Leonard SW, Mondia JP, Van Driel HM, et al. Tunable two-dimensional photonic crystals using liquid crystal infiltration. Phys Rev B 2000;61:R2389.
[56] Chang ASP, Morton KJ, Tan H, et al. Tunable liquid crystal-resonant grating filter fabricated by nanoimprint lithography. IEEE Photonics Technol Lett 2007;19:1457–9.
[57] Song JL, Wu H, Cheng Q, et al. 1D trilayer films grating with W/SiO2/W structure as a wavelength-selective emitter for thermophotovoltaic applications. J Quant Spectrosc Radiat Transfer 2015;158:136–44.
[58] Song JL, Si MT, Cheng Q, et al. Two-dimensional trilayer grating with a metal/insulator/metal structure as a thermophotovoltaic emitter. Appl Opt 2016;55:1284–90.
[59] Shuai Y, Tan HP, Liang YC. Polariton-enhanced emittance of metallic–dielectric multilayer structures for selective thermal emitters. J Quant Spectrosc Radiat Transfer 2014;135:50–7.
[60] Moharam MG, Grann EB, Pommet DA, et al. Formulation for stable and efficient implementation of the rigorous coupled-wave analysis of binary gratings. JOSA A 1995;12:1068–76.
[61] Liu V, Fan S. S4: A free electromagnetic solver for layered periodic structures. Comput Phys Commun 2012;183:2233–44.
[62] Zhao B, Wang L, Shuai Y, et al. Thermophotovoltaic emitters based on a two-dimensional grating/thin-film nanostructure. Int J Heat Mass Transfer 2013;67:637–45.
[63] Liu X, Zhao B, Zhang ZM. Enhanced near-field thermal radiation and reduced Casimir stiction between doped-Si gratings. Phys Rev A 2015;91:062510.
[64] Mayer J, Gallinet B, Offermans T, et al. Diffractive nanostructures for enhanced light-harvesting in organic photovoltaic devices. Opt Express 2016;24:A358–73.